CrossMark

RESEARCH PAPER

Friction spot joining (FSpJ) of aluminum-CFRP hybrid structures

S. M. Goushegir[1]

Abstract The employment of various materials (such as light-weight metal alloys and composites) with distinct physico-chemical properties in the automotive and aerospace industries has opened a new field of research into the joining of dissimilar materials. Several alternative methods have recently been developed for joining metal-composite multi-material structures. Friction spot joining (FSpJ) is an innovative technique within welding-based joining technologies suitable for metal-composite structures. This work aims to address and overview different aspects of FSpJ. Case-study overlap joints using aluminum alloy AA2024-T3 and carbon-fiber-re-inforced poly(phenylene sulfide) (CF-PPS) were produced. Peak temperatures of up to 474 °C were recorded during the process. Such temperatures are well below thermal decomposition of PPS, and extensive thermal degradation of PPS was not detected by thermal analysis in this work. Microstructure analysis was performed showing usual metallurgical phenomena (recovery and dynamic re-crystallization) taking place with friction-based aluminum joining. Microstructural changes caused an alteration to the local mechanical properties as confirmed by microhardness and nanohardness measurements. Moreover, microstructural analysis of the composite part revealed the formation of a small number of volumetric defects such as pores and fiber-matrix debonding. Bonding mechanisms at the interface were studied into details by microscopy analysis and X-ray photoelectron spectroscopy. The influence of various aluminum surface pre-treatments on the bonding mechanisms and mechanical performance of single-lap shear joints was studied. In addition, fatigue life of the joints was investigated using an exponential model to obtain S-N curves. Finally, the quasi-static strength of the friction spot joints was compared with the state-of-the-art adhesive bonding. Friction spot joints showed 50 % stronger joints than adhesively bonded joints, indicating the potential of the technique to be used for joining lightweight metals to composite materials.

1 Introduction

The requirements of modern society have changed over the centuries and particularly in the last few decades. Reliable and safe structures with high-performance, new-energy source, and environmentally friendly sustainable products and processes are some of the demands in this new era. In addition, as a result of globalization, rapid transportation has become a major requirement with the need for travel and the export of goods and services around the world. Furthermore, environmental protection is now a major concern. Reduction in emissions of greenhouse gases (such as carbon dioxide), particularly from vehicles by weight saving and cleaner fuel consumption, helps circumvent negative environmental impacts. Such requirements and concerns have motivated scientists and engineers in scientific communities and industrial sectors to design lightweight yet mechanically strong and reliable structures. Lightweight structures are nowadays increasingly in demand for a wide range of engineering applications, such as the transport industry [1–3], wind power [4], and bridge construction [5]. Especially in the transport industry, where energy efficiency is required, the use of high-performance polymers and their respective composites, such as carbon-fiber and glass-fiber-re-inforced polymers (CFRP and

✉ S. M. Goushegir
mgoushegir@gmail.com

1 Helmholtz-Zentrum Geesthacht, Centre for Materials and Coastal Research, Institute of Materials Research, Materials Mechanics, Solid State Joining Processes, Geesthacht, Germany

Springer

GFRP), has been emerging in the design of hybrid, multi-material structures. This is primarily due to their inherent capacity to reduce the weight of an engineering structure, such as an aircraft or car. In addition to the lightweight character of composites, they possess outstanding corrosion resistance, environmental stability, high strength, and high fatigue performance, making them attractive for a variety of industries [6, 7]. In addition, advanced lightweight metals such as aluminum, titanium, and magnesium alloys are being further developed to reduce the weight of a structure while maintaining high mechanical performance. The development and employment of different materials with a diverse range of properties helps designers to select the right combination of materials to fulfill the required properties of the desired structure [6].

New generation aircraft, e.g., Boeing 787 Dreamliner and Airbus A350 XWB, are examples of large multi-material structures. In both aircraft, approximately 50 wt.% composites are mixed with 50 wt.% lightweight metal alloys such as aluminum [8, 9]. In addition to the aircraft industry, automotive manufacturers intend to use more polymers and composites in the bodies of their cars [10–14]. Recently, it was stated that by 2030, in the USA, polymers and composites will be the primary materials used by the automotive industry to fulfill its demands [12]. Thus, more material mixing is expected in automobiles in the near future. The Mercedes-Benz F125 research vehicle [15] is an example of a new concept under development for the year 2025 and beyond. The car will consist of metal-polymer hybrid structures to reach its goal of emission-free mobility.

Despite the benefits of using different lightweight materials in a structure, the joining of dissimilar materials such as metal alloys and composites presents a great challenge due to their distinct physicochemical properties [2]. Amancio and dos Santos [16] have categorized various joining technologies for metal-polymer hybrid structures; these range from more conventional adhesive bonding and mechanical fastening to new welding-based technologies. Nevertheless, traditional bonding and mechanical fastening exhibit technological and environmental limitations. For instance, the curing time of an adhesive for structural adhesive bonding is a major shortcoming. In addition, bonding of thermoplastic composites requires special pre-treatments to increase the intrinsic adhesion between the composite and the adhesive to improve the wettability and surface tension of the thermoplastics [17]. Problems in the

mechanical fastening of metal-composite joints have also been reported for the Airbus A380 [6]. During the development phase of the A380 wing, composite ribs were joined to the metal skin by bolting on aluminum brackets. During the operation, some cracks appeared in the brackets, which could have led to failure of the entire component. Such technical limitations have motivated recent investigations into alternative and advanced joining technologies suitable for hybrid structures, to overcome or reduce the drawbacks of conventional techniques.

Friction spot joining (FSpJ) is an alternative joining technology for producing metal-composite joints, patented by Helmholtz-Zentrum Geesthacht, Germany [18]. As the name implies, FSpJ belongs to friction-based joining and welding technologies. The new technology was developed as a variant of the Friction Spot Welding (FSpW) of metals [19]. This work aims to address and review the fundamental scientific and technological aspects of the FSpJ process. Case-study joints were produced using transport-grade lightweight aluminum alloy AA2024-T3 and carbon-fiber-reinforced poly(phenylene sulfide) (CF-PPS). Various experimental and analytical techniques were employed to investigate different properties of the joints. These include microstructural changes of the joining parts, process-related physicochemical alteration of the composite, local mechanical properties, global mechanical performance of the joints under static and dynamic loading, and the influence of aluminum surface pre-treatments on the interface of the friction spot joints.

2 Principles of the FSpJ

2.1 FSpJ tool

In the FSpJ process, a non-consumable tool consisting of three parts is used to generate frictional heat. The tool includes a clamping ring, sleeve, and pin, which are mounted coaxially and can be moved independently of each other (Fig. 1). The clamping ring is the external component of the tool that is used to hold the parts to be joined together during the process against a backing bar. The pin and sleeve can move vertically and rotate independently. They produce the required heat as a result of the friction between these parts and the metal [20].

Fig. 1 Illustration of the FSpJ tool; **a** consisting of three parts (dimensions in mm) and **b** tool parts coaxially mounted together. Reproduced with permission from [21]
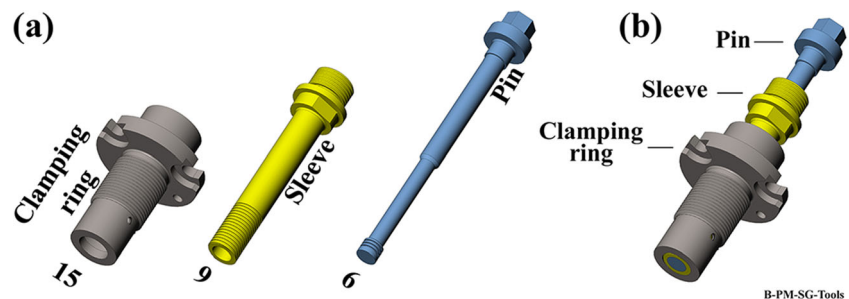
Fig. 2 Configuration of the joining parts and the FSpJ tool before the process starts
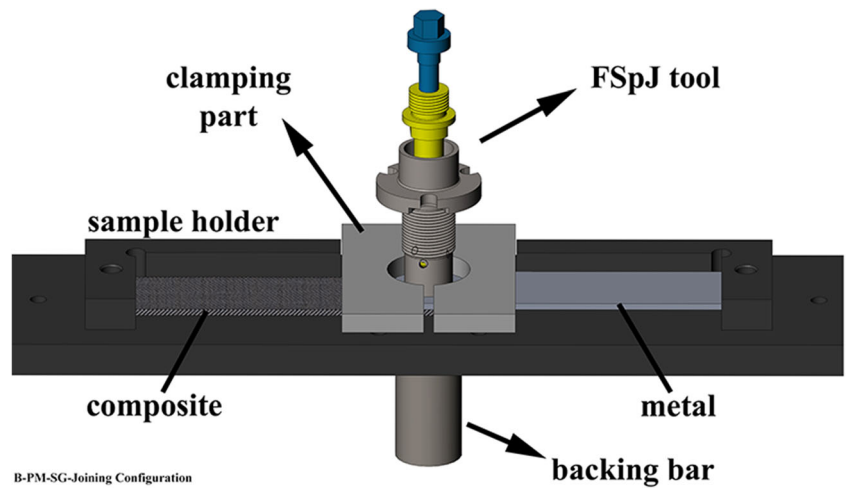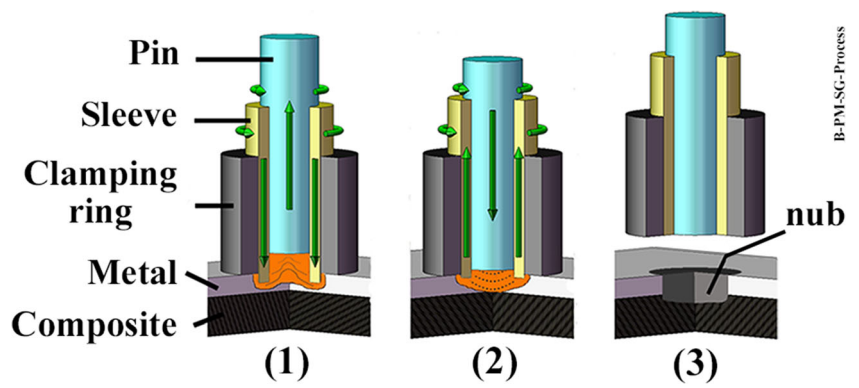

Fig. 3 Schematic representation of the FSpJ process steps; *1*, the sleeve plunging plasticizes the metal; *2*, spot refilling; and *3*, joint consolidation. Adapted from [20]

2.2 FSpJ process

Before the process starts, the sheets to be joined are held together in an overlapping configuration on a sample holder, using a clamping device. The parts are kept clamped during the whole process to avoid any separation of the sheets during the cooling phase. This is due to the large differences in coefficients of thermal expansion and shrinkage behavior of metal and polymer. Next, the tool approaches the top sheet (in this case a metal alloy) and the joining parts are fixed by the clamping ring against a backing bar, through the application of the joining pressure. Figure 2 illustrates the configuration of the joining parts before the process starts.

The FSpJ process can be divided into three main steps [20]. There are two possible variants for the FSpJ technique: "Pin Plunge" and "Sleeve Plunge" [20]. In the sleeve plunge variant, the first step of the process starts when the rotating sleeve plunges into the metallic sheet at a pre-defined position and the pin retracts upwards. Due to the friction between the rotating sleeve and the metal, the temperature rises locally in a volume around the tool but below the melting point of the metal. This causes local softening and plasticizing of the metal alloy. The plasticized metal alloy flows into the reservoir left behind by retraction of the pin (Fig. 3 (1)). As a second step, the pin is pushed against the softened metal to refill the keyhole left in the metallic sheet that was created by the plunging sleeve (Fig. 3 (2)). Finally, the tool is retracted and the joint consolidates under cooling and pressure (Fig. 3 (3)). Note that the tool only plunges into the metal part to a shallow depth that does not reach the composite interface, to avoid any damage to the load-bearing network of fibers. Figure 4 depicts the top view of a sound metal-composite FSp joint.

Fig. 4 Top view of a sound metal-composite FSp joint (AA2024/CF-PPS). Adapted from [22]
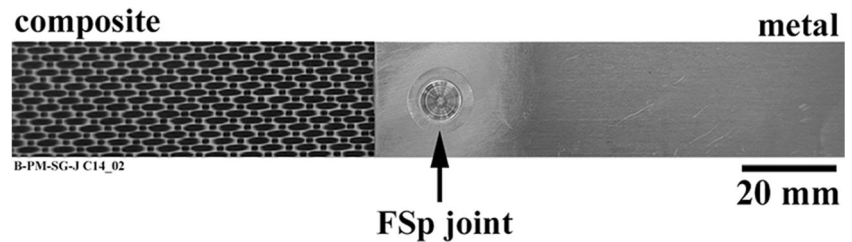
Fig. 5 Example of a cross-section of an FSp joint in the middle of the spot. The *rectangle* indicates the nub (AA2024/CF-PPS). Adapted from [24]
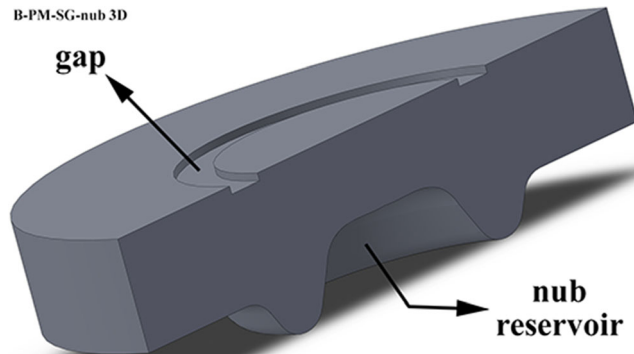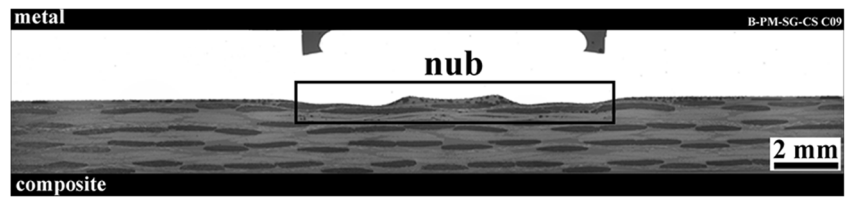

Fig. 6 Schematic illustration of the cross-section of the middle of the spot area. A nub reservoir is formed which accommodates the molten polymer. The composite partner is omitted for better visualization

physicochemical differences of metal and polymer parts, which usually lead to sharp interfaces.

During the joining process, high temperatures around the tool increase the local formability of the metal. For this reason, the plasticized metal is deformed by the plunging motion of the sleeve and the pin and it creates a geometrical undercut in the form of a "nub" [20]. As a result of the axial force exerted by the tool, the nub is slightly inserted into the composite and this increases mechanical interlocking between the joining parts. Figure 5 shows the cross-section of an FSp joint in the middle of the spot, where the nub is indicated by a black rectangle. A reservoir is created in the center of the nub where the composite is entrapped and accommodated inside. The nub reservoir is also indicated in a 3D graphical view of the spot area in Fig. 6 (without the composite partner to aid visualization).

In the pin plunge variant, the pin penetrates into the metal piece while the sleeve is retracted [20]. The other process steps are equivalent to the sleeve plunge variant. As the area of the sleeve is larger than the area of the pin, it can be assumed that in the sleeve plunge variant, the bonding area is bigger, resulting from a higher heat input, and hence better mechanical performance will be achieved. The sleeve plunge variant is used throughout this paper to explain the process.

It is worth mentioning here that there are three main differences between FSpJ and FSpW [23]. Firstly, unlike the FSpW of metals and thermoplastics, with FSpJ, the tool only plunges to a shallow depth in the metallic part and does not reach the composite. The reason for this is to avoid excessive degradation of the matrix of composite and damage to its network of load-bearing fibers. Secondly, with FSpJ, the adhesion forces from creation of a molten layer act as one of the main bonding mechanisms. However, atomic diffusion (in metal spot welds) and molecular interdiffusion (in thermoplastic spot welds) are the main mechanisms leading to weld formation. Furthermore, in FSpJ material mixing does not happen due to the huge

In the course of the joining process, the frictional heat generated is transferred from the metal alloy to the composite interface via conduction. Resulting from the very low thermal conductivity of the composite, this heat is accumulated at the interface and leads to a local increase of the temperature. Since the temperature exceeds the melting or glass transition temperature of the composite's matrix, a thin layer of the molten or softened polymer forms in the spot area. A part of the molten layer is squeezed out and flows laterally throughout the overlap region as a result of the axial pressure exerted by the tool. The molten layer is then consolidated under pressure, whereby it induces adhesion forces between the metal and the composite. The total bonding area in the FSpJ corresponds to the outer periphery of the consolidated molten layer, as shown in Fig. 7. Figure 7a depicts the presence of adhesion forces between metal and composite inside the bonding area. A fracture surface of the joint after lap shear testing is also illustrated in Fig. 7b where the total bonding area is indicated by the dashed circle on the metal part.

Fig. 7 a Illustration of the adhesion forces as one of the primary bonding mechanisms in FSpJ and b an example of the fracture surface of an FSp joint tested by lap shear (AA2024/CF-PPS)
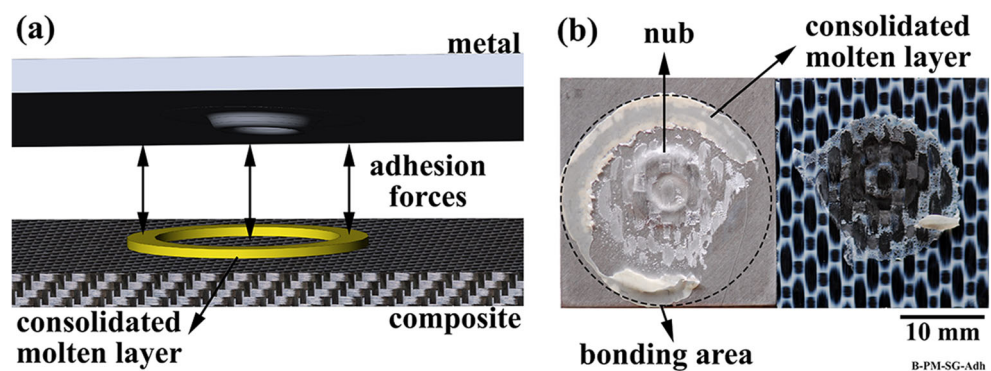
2.3 Process parameters

Similar to the FSpW of metals [25, 26], there are four primary process parameters in FSpJ [20, 22, 27]: rotational speed (RS) of the plunging sleeve, sleeve plunge depth (PD) into the metal alloy, joining time (JT), and joining pressure (JP). The process parameters affect the bonding mechanisms, microstructure, and therefore the mechanical performance of the joints. RS controls the heat input and temperature evolution during the joining cycle. Due to the temperature changes, the local microstructure of the metal part is influenced by the process. Furthermore, the amount of molten polymer generated is directly related to the heat input and hence the RS of the sleeve. Moreover, the viscosity of the molten polymer, its rheological behavior as well as the formation and extent of defects in the composite are all temperature-dependent phenomena that are influenced indirectly by RS. JT, which includes sleeve plunging time and retraction time, governs the joining speed. It also contributes to the amount of the heat input into the process and the extent of temperature development around the tool. Similar to RS, the above-mentioned temperature-dependent phenomena are also affected by JT. Another important function of RS and JT is to indirectly control the shape of the metallic nub, since the generation of more frictional heat increases the local formability of the metal. PD of the sleeve has a forging function and is mainly responsible for the shape and inserted depth of the nub into the composite. Higher PD usually leads to a deeper indentation of the deformed metal into the composite, thus better macro-mechanical interlocking between the parts, as recently reported in [22, 27]. JP is a parameter with the main function of controlling the flow of the molten polymer. An exerted axial force on the spot area as a result of the applied joining pressure influences the lateral flow of molten polymer. The combination of heat input and JP influences the flow and the bonding area as explained in [22]. In addition, an intimate contact between the molten polymer and the metal at the interface depends on the applied JP. This is especially important when the surface of the metal is rough, for instance resulting from surface pre-treatment. Complete filling of asperities in the metal surface by the molten polymer by applied JP leads to an increase in micromechanical interlocking and hence mechanical performance of the joints.

2.4 Advantages and limitations of FSpJ

The main advantages of FSpJ are listed below:

a) Short joining cycles: the joining time in FSpJ varies between 2 and 8 s depending on the metal alloy and the polymer or composite in use [20], which is much faster than state-of-the-art adhesive bonding.

b) Weight saving: because in FSpJ no obligatory use of additional material (such as fillers or rivets) is necessary to that of the joining parts, no additional weight is added to the structure.

c) Absence of through holes: unlike traditional mechanical fastening techniques, there is no need to pre-drill a hole with FSpJ. This is especially important in cases of continuous fiber-reinforced composites, because these materials are usually highly susceptible to cracking as a result of drilling, which deteriorates their local mechanical strength leading to premature failure of the joint.

d) Environmentally sound: the process is green and environmentally friendly, because there are no emissions generated during or after the joining cycle [20].

e) Reparability: since thermoplastics (as one of the joining parts) can withstand being re-melted and solidified several times, the joints may be repaired on the same spot (a preliminary result is given in [28]).

f) Recyclability: the joints can be recycled by separating the joining parts. The joint can be heated above the melting temperature of the thermoplastic, to separate the metal from the composite.

g) Joining over sealant: in real-life applications, joints are normally sealed against corrosion and environmental effects. If joining can be performed over a pre-applied sealant (e.g., by the addition of a film interlayer as shown in [29]), the time and required effort for post-application of sealant is reduced.

h) Low-cost machinery: the equipment required for production use of FSpJ is the same as the available FSpW machine, and no further alteration or adaptation is required [20].

Besides the main advantages that FSpJ offers, there are several limitations of the process as follows:

a) Joint geometry: only overlap configuration joints can be produced with FSpJ [20].

b) Disassembling: since the joining parts are physically and chemically bonded, there is no possibility of disassembling and re-assembling the joints without damaging the structure.

c) Low torsion and peeling strength: similar to adhesive bonding, FSp joints are mainly capable of bearing a shear loading, but the torsion and peeling strengths of the joints are relatively low.

d) Thickness of metal sheet: due to local mechanical deformation of the metal (nub area) and the possibility of defective joint formation, thin metallic sheets (e.g., less than 1 ml for engineering aluminum alloys) cannot be FSp joined with present knowledge.

Table 1 Nominal chemical composition of AA2024-T3 used in this work

Element	Si	Fe	Cu	Mn	Mg	Cr	Zn	Ti	Al
wt.%	0.1	0.17	4.55	0.45	1.49	<0.01	0.16	0.021	Bal.

3 Experimental

3.1 Materials and joining procedure

Rolled sheets of aluminum alloy AA2024-T3 with a thickness of 2 mm (supplied by Constellium, France) were used as the metallic partner for FSpJ throughout this work. This alloy is mainly used in the primary structures of aircraft. AA2024 is an alloy suited to precipitation hardening with Cu and Mg as its main alloying elements. Heat treatment (T3) leads to the formation of strengthening phases such as Al_2CuMg and $CuAl_2$, which give rise to the high strength of this alloy [30]. The alloy exhibits a high strength-to-weight ratio, good fatigue resistance and damage tolerance, high fracture toughness, as well as good formability [31]. Table 1 lists the nominal chemical composition of the AA2024-T3 alloy used in this work, which was determined by chemical analysis.

CF-PPS with a 2.17-mm nominal thickness consisting of five harness-woven quasi-isotropic laminates (supplied by TenCate, the Netherlands) with 50 vol% fibers (42 wt.% fibers) was used as the composite partner for FSpJ. The composite consists of seven plies of carbon fibers in the following sequence: $[(0.90)/(\pm45)]_3/(0.90)$. CF-PPS is considered a high-performance semi-crystalline thermoplastic composite that is mainly used in primary and secondary aircraft parts, because of its high strength, rigidity, chemical resistance, and low water absorption [32–34].

Friction spot joints were produced in a displacement-controlled equipment (RPS100, Harms & Wende, Germany) using sleeve plunge variant. Prior to the joining process, the composite parts were cleaned in an acetone ultrasonic bath for 3 min and dried in air. The aluminum parts were wiped with acetone to remove loose surface contaminations. Further, some of the aluminum specimens were pre-treated with a variety of procedures. For a detailed information about surface pre-treatments, refer to [28]. After cleaning the specimen, the aluminum part was placed above the composite in an overlap configuration against the sample holder. At the end of the joining process, an experimental consolidation time (intentionally extended to times above the minimum time required for polymer consolidation, to ensure the complete absence of differential contraction) of 1 min was selected for the joining conditions. During the consolidation time, pressurized air (flow rate, 22.9 l/min) was blown continuously over the joint. Finally, the joint was removed from the clamping system for further analysis.

Statistical analysis was performed using full-factorial design of experiments and analysis of variance. Resulting from the statistical analysis, a set of joining parameters (RS, 2900 rpm; PD, 0.8 mm; JT, 4 s; JP, 0.3 MPa) was achieved which optimized the strength of the single overlap FSp joints. This optimized set of parameters was used in this work to produce FSp joints and evaluate their properties. The results of process optimization and the influence of process parameters on the mechanical strength of friction spot joints were published in a separate manuscript [22].

3.2 Temperature measurement

Temperature development during the FSpJ process was monitored by thermometry and infrared (IR) thermography. A chromium–nickel-type K thermocouple (TC; with a diameter of 0.7 mm) was used for thermometry, to measure the local temperature of the polymer molten layer at the interface. A hole of 0.8 mm was drilled at the bottom of the composite reaching to the interface with the aluminum to set up the thermocouple. A data acquisition system connected to the thermocouple was used to collect the measured data at the rate of 50 Hz.

Moreover, an infrared thermographic camera (VarioTHERM, Jenoptik, Germany) was used to monitor temperature changes on the surface of the aluminum during the joining cycle. The monitoring process was carried out in the range of 150 to 700 °C with a resolution of 256 × 256 pixels at 50 Hz. Figure 8a illustrates the position of the infrared camera in relation to the joining

Fig. 8 Schematic illustration of temperature measurement by IR thermography; **a** showing the position of the IR camera and **b** an example of a snapshot from the peak temperature on the aluminum surface during FSpJ. The area used to measure the temperature is indicated in the snapshot
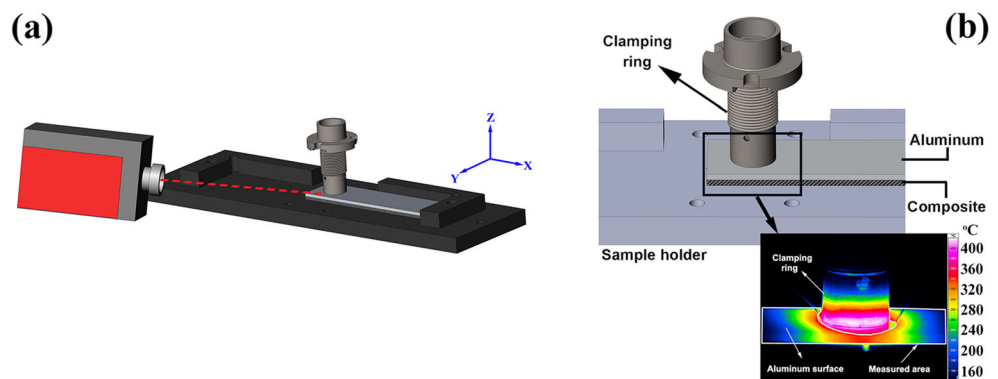
parts. The camera was inclined approximately 15° both in *x* and *z* directions to be able to capture the temperature on the aluminum surface through the whole bonding area. Besides, Fig. 8b illustrates the measurement set up and the position where the temperature was captured on the surface of the aluminum. This figure also shows a snapshot of a thermograph in which the measurement area is indicated. The peak temperature in the selected area was reported as the process temperature. Prior to capturing the temperature, the aluminum parts were painted with black paint to reduce any measurement errors as a result of the light reflection.

3.3 Thermal analysis—thermogravimetry

Thermal analysis of the composite part in the FSp joints was carried out in order to evaluate the local physicochemical changes in the composite as a result of the FSpJ process. The composite base material was also characterized as a reference for comparison with the composite in the joints. Thermogravimetry (TG) was performed using Netsch TG 209F3 Tarsus® equipment.

In this work, PPS was extracted from the consolidated molten layer on the aluminum side of the fractured joint with the aid of a scalpel. Figure 9 shows the position of the PPS extracted for the thermal analysis. In addition, PPS from the composite was also extracted from pieces of the base material.

To conduct the experiments, a mass of 10 mg of the extracted PPS was placed in aluminum oxide crucibles. A heating rate of 20 K/min was selected in the temperature range of 25–800 °C for obtaining the PPS mass change over temperature. Inert nitrogen gas with a flow rate of 250 ml/min was used as the purge gas to investigate the thermal decomposition of the PPS.

TG was calibrated before the experiments, and ASTM standard E1131-08 [35] was followed to perform the analysis.
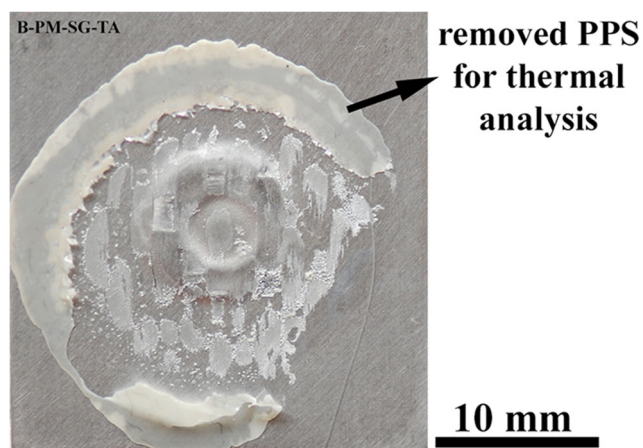

Fig. 9 Consolidated PPS layer that remained attached to the aluminum after mechanical testing was removed and used for thermal analysis

3.4 Microstructural and fracture surface analysis

To analyze the microstructure of the joints and the fracture surfaces after mechanical testing, light optical microscopy (LOM; DM IR microscope, Leica, Germany), laser scanning confocal microscopy (LSCM; VK-9700, Keyence, Japan), and scanning electron microscopy (SEM; Quanta™ FEG 650 equipment) were employed. The cross-section of the joints at the center of the spot joint was analyzed by LOM, to reveal the joint's microstructure. Standard materialography procedures were followed to prepare the samples for LOM. The joints were cut in the middle of the spot and embedded in cold resin. The embedded specimens were ground and polished following standard procedures to obtain a smooth surface suitable for LOM. In order to reveal the microstructure of the aluminum in the joints, electrochemical etching (30 V, 120 s, room temperature) in Barker solution (200 ml water and 5 ml fluoroboric acid) was carried out.

Where necessary, SEM was used to reveal the detailed microstructural features of the joints. In this case, a voltage of 5 kV, spot size of 3, and a working distance of 10 mm were used. For fracture surface analysis, the working distance of 15 mm was set. Before analyzing the samples, their surfaces were gold sputtered using a Q150R ES equipment (Quorum Technologies Ltd., England) for 30 s with a current of 65 mA to make them conductive.

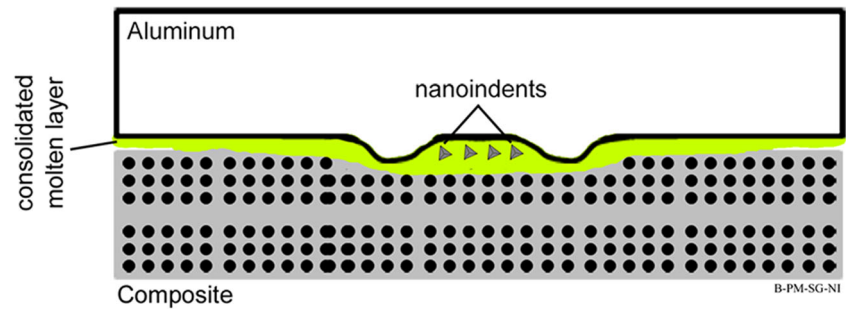### 3.5 Local mechanical properties

3.5.1 Microhardness

A microhardness investigation was carried out on the aluminum from the cross-section of the joints, prepared similar to the LOM specimens, to analyze the local mechanical properties of the aluminum in the joints. The measurements were performed using Vickers Zwick/Roell indenter equipment and followed the ASTM E384-992e1 standard [36]. A microhardness map was obtained from one half of the specimen (due to the symmetry in the FSp joint) by applying an indentation load of 200 g for 10 s. The distance between the indents was 300 μm.

3.5.2 Nanoindentation

When it came to the composite, the presence of pores and voids in the consolidated molten PPS particularly close to the interface with the aluminum in addition to a relatively high volume fraction of fibers made it almost impossible to employ microhardness. The area of the microhardness indenter was relatively large, which in most of the cases partially touched fibers or pores, leading to inaccurate values of the hardness. For this reason, nanoindentation was selected to evaluate the local mechanical properties of the composite in the joints.

The nanoindentation experiments were carried out using a Nano Indenter® XP (Agilent Technologies, USA) with a load

capacity of 10 N. For the experiments, a Berkovich diamond indenter was employed. A maximum indentation depth (h_{max}) of 1 μm was fixed and the maximum indentation load (P_{max}) corresponding to the maximum indentation depth was recorded. The continuous stiffness measurement (CSM) method was used to monitor the stiffness while the indenter was being driven into the specimen. Both hardness and stiffness of the PPS matrix were then calculated and reported as the results of the nanoindentation experiments.

Nanoindentation was performed on the polished cross-section of the joints from the center of the spot joints and prepared according to the standard materialography procedures. Figure 10 illustrates the position of the indentations in the joints. The indents were positioned in the consolidated PPS molten layer, close to the interface with the aluminum. Note that the indents are sketched larger than to scale for better visibility. Between seven to ten indents were distributed in the consolidated molten layer in the middle of the joint. In the CF-PPS base material, the indents were positioned in the PPS matrix, far from the carbon fibers at different positions.

3.6 X-ray photoelectron spectroscopy for interface analysis

X-ray photoelectron spectroscopy (XPS) was carried out using a Kratos DLD Ultra Spectrometer with an Al-Kα X-ray source (monochromator) operated at 225 W. A pass-energy (PE) of 40 eV was used for the region scans. The spectra of clean surfaces (contamination from environment removed) were calibrated to 284.8 eV binding energy of the C1s signal. For all the

samples, a charge neutralization was necessary. The processing and mathematical treatment were carried out using CasaXPS V.2.3.16 software. Smoothing of the data in region files was carried out for low signal-to-noise ratios. Depth profiling was carried out using argon sputtering with a beam energy of 3.8 keV and a current density of 120 μA/cm^2. The etching rate was calibrated to 10 nm/min using Ta_2O_5.

3.7 Global mechanical properties

3.7.1 Single-lap shear testing

Single-lap shear (SLS) testing was carried out as the main method to analyze mechanical performance of the joints throughout this work. The SLS joint geometry is widely used in the literature by researchers to study joint mechanical performance, due to its geometrical simplicity. The SLS strength of the joints was evaluated according to the ASTM D3163-01 standard [37] using a universal testing machine (Zwick Roell model 1478) with a load capacity of 100 kN. The traverse test speed was 1.27 mm/min, and the tests were performed at room temperature. Three to five replicates were used to obtain the average ultimate lap shear force (ULSF) of the joints. The ULSF obtained is the peak force that a joint can bear before final failure. Aluminum and composite specimens with dimensions of 100 × 25.4 mm were machined for joining and subsequent single-lap shear testing. The overlap area of the joints was 25.4 × 25.4 mm. For mechanical testing, a free distance of 150 mm between the grips was used. Figure 11 shows the SLS geometry of the joints and its dimensions used in this work.

Fig. 11 **a** Schematic illustration of the SLS joint geometry; the respective dimensions used in this work from **b** side view and **c** top view. All dimensions are in millimeters
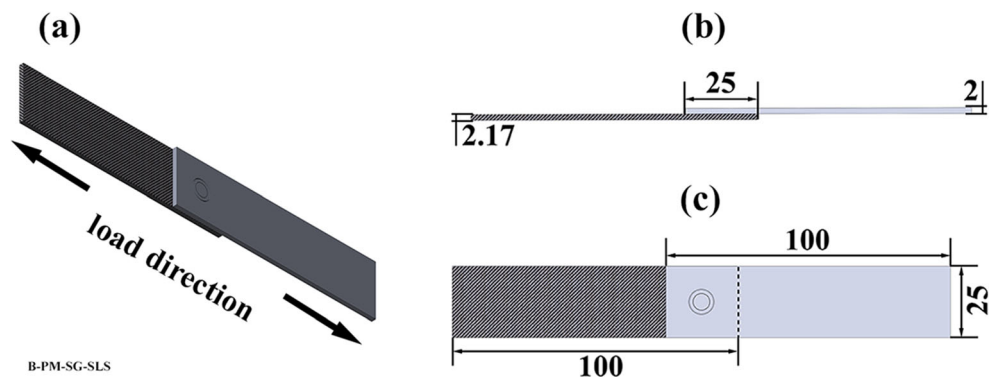
3.7.2 Fatigue experiments

Fatigue experiments of the FSp joints were performed using SLS joint geometry. The experiments were carried out under constant amplitude at a frequency of 5 Hz using load-controlled servo-hydraulic equipment with a load capacity of 25 kN. A tension-tension load ratio (minimum to maximum applied cyclic load) of $R = 0.1$ was selected to perform the experiments. All the experiments were carried out at room temperature. Different load levels (maximum applied cyclic load) were selected to obtain fatigue lives between approximately 10^3 and 10^6 cycles. A minimum of two specimens for each load level were tested. To align the SLS joints, end tabs with dimensions of 40×25 mm were machined and attached to the specimens. Two rivets were used to fix the joint in the grips of the testing machine. For this purpose, a hole was drilled in each side of the joint at a distance of 27 mm from the edge. A free length of 95 mm was used during the fatigue experiments. Figure 12 displays the geometry of the joints and its dimensions for fatigue testing used in this work.

4 Results and discussion

4.1 Temperature development

Temperature development is of utmost importance since it gives information about temperature-dependent phenomena taking place in the course of the joining process such as metallurgical changes in the aluminum, possible degradation of the composite, formation of defects, etc.

The whole range of temperature development (using different joining parameters) on the surface of the aluminum measured by IR thermography is reported in [22]. The results showed a variation between 345 and 474 °C. For the optimized joining condition, the peak process temperature was 437 °C, being approximately 87 % of the aluminum incipient melting temperature of 502 °C [31]. It was reported [25] that a temperature of approximately 400 °C lies in the range of dynamic re-crystallization of AA2024 for friction-based joining processes. So, metallurgical transformations such as re-

crystallization of the grains are expected in the aluminum in the vicinity of the tool, which will be explained later.

In addition to temperature measurement of the aluminum part, a thermocouple was also used to measure the temperature of the molten PPS layer at the interface between the aluminum and CF-PPS. The average temperature obtained at the interface was 418 °C, much higher than the melting point of PPS (280 °C). Since the temperature of the molten PPS at the interface below the tool is expected to be higher than the rest of the interface, the temperature measured by the thermocouple can be used to explain any physicochemical changes or possible degradation on the PPS.

4.2 Process-related physicochemical changes in the CF-PPS

Thermal effects in polymers and composites, such as alteration of the amount of crystallinity, morphology of crystals, and the extent of thermal degradation are temperature dependent. In high-temperature processes, such as welding and joining, an understanding of the physicochemical changes induced by the process is crucial, since local and global mechanical properties of the material depend on its physicochemical state. For this reason, TG analytical technique was used to study the physicochemical properties of the affected zone in CF-PPS as a result of the FSpJ process.

Figure 13 shows the TG curves for CF-PPS as base material (BM) prior to the joining process, as well as after the FSpJ process (joint) between 30 and 800 °C. The onset temperature of decomposition was obtained and resulted in 511.7 ± 4.5 °C for BM and 514.5 ± 0.5 °C for the joint. The result obtained for the BM is in agreement with those reported in the literature for the onset decomposition of PPS [38–42]. As described earlier and reported in [22], the range of process peak temperatures achieved in this work was between 345 and 474 °C, being 418 °C at the interface. The peak temperature of the PPS at the interface is far below the onset decomposition temperature of CF-PPS. Thus, extensive thermal degradation of the PPS, such as decomposition, main chain scission, or carbonization as a result of the process is not expected.

Fig. 12 **a** Schematic illustration of the geometry of the fatigue specimen; the respective dimensions used in this work from **b** side view and **c** top view. All dimensions are in millimeters
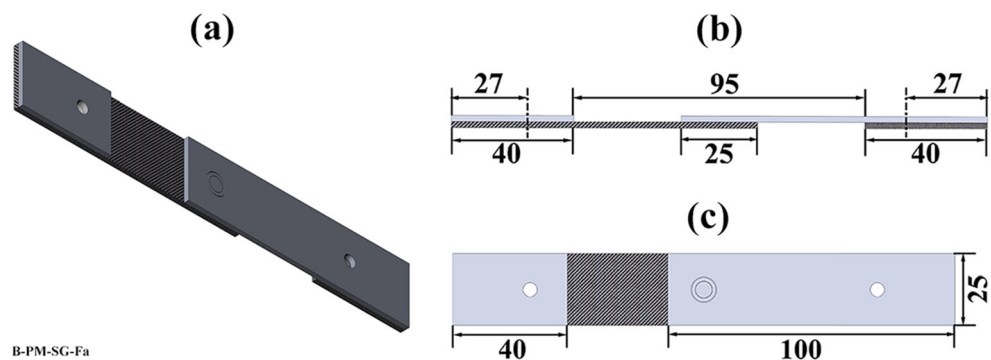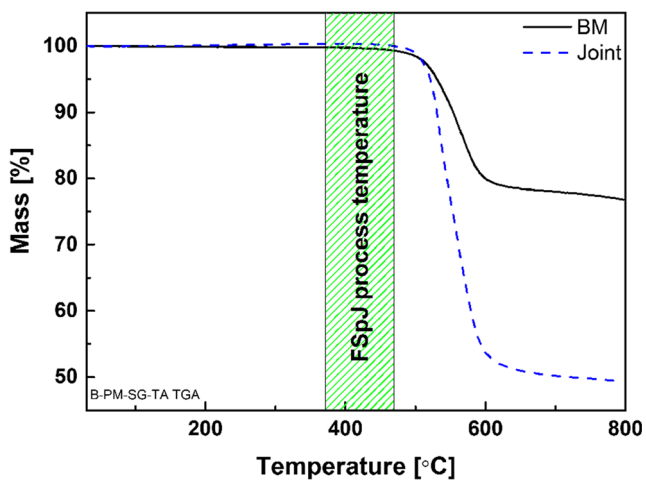
Fig. 13 TG analysis of the PPS in the BM and the joint in nitrogen showing the mass change between 30 and 800 °C. The *green area* shows the window of the FSpJ process temperature

Furthermore, it is reported that increasing the heating rate in the TG experiments shifts the onset degradation to higher temperatures, for instance, for PMMA [43] and PA 66 [44]. This is probably due to a delay in the beginning of chain motion. At a high heating rate, the chains do not have enough time to react to the high temperatures. Since the heating rate in FSpJ (approximately 355 °C/s) is much faster than the 20 °C/min used in the TG experiments, it is believed that the actual onset decomposition temperature would have been far more than the temperatures obtained, if the TG scanning had been done using this process heating rates. This further supports the assumption that extensive thermal degradation (decomposition) does not occur with the studied process parameter range and base materials. Changes in molecular weight, indicating thermal degradation (both by chain scission or cross-linking) may take place. However, this was not the focus of this work, particularly considering that the process did not lead to decomposition (excessive thermal degradation).

In addition to the TG curve, a derivative thermogravimetry (DTG) curve helps to indicate the degradation stages and the temperature at which the rate of decomposition is maximum. Figure 14 depicts a part of the TG curves (in green) in the range of 400–700 °C along with the respective DTG curves (in blue) for BM and the joint. It is obvious from the DTG curve that weight loss and thermal degradation for the CF-PPS occurs at one stage with its maximum rate at about 566 °C. This result agrees with the literature for instance the studies by Bo et al. [38] and Day and Budgell [45]. In contrast to the BM, CF-PPS from the joint showed a two-step degradation obtained by DTG curves. The peak at above 560 °C is close to the single peak from the BM, suggesting the same degradation mechanisms such as pyrolysis or main chain scission. The appearance of another peak at 534.6 °C for the joint may be attributed to slight cross-linking of the PPS molten layer. It was reported that intermolecular branching, similar to cross-linking in PPS, may
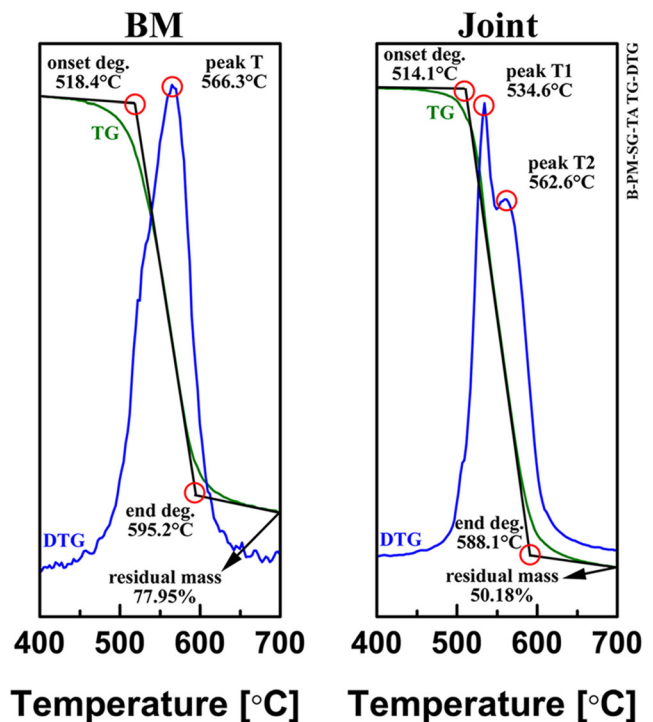

Fig. 14 TG-DTG curves for the BM and the joint in the range of 400 to 700 °C. The BM showed one-step degradation, whereas the joint showed two-step degradation as indicated by the two peaks in the DTG curve

occur at temperatures above 300 °C in air [46]. Therefore, slight cross-linking in the consolidated molten PPS layer may take place during the FSpJ process. The cross-linked part of the PPS may then start to degrade at a separate stage, leading to the formation of a new peak in the DTG curves.

4.3 Microstructural zones in FSpJ

Microstructural zones form in an FSp joint due to the interaction of the tool with the metal, generating frictional heat and a local rise of temperature, and the amount of the heat conducted from the metal to the composite. Generally, the microstructural zones can be divided into four areas: metal stir zone (MSZ), metal thermo-mechanically affected zone (MTMAZ), metal heat-affected zone (MHAZ), and polymer heat-affected zone (PHAZ).

The microstructural zones on the aluminum are very similar to those reported for FSpW of AA2024 [25] and AA6181 [47]. The microstructural zones in FSpJ are shown in Fig. 15, in which Fig. 15a shows an overview of the microstructure and Fig. 15b–f illustrates the detailed microstructure of each zone. Figure 15b, c compares the microstructure of the base material (BM) and MTMAZ, respectively. The microstructure of the AA2024 in the MTMAZ is influenced by the relatively high temperature attained during the process as well as severe deformation [25, 47]. This zone forms in a volume close to the plunging sleeve where the aluminum grains are affected by

Fig. 15 Microstructural zones that form in the aluminum. **a** General overview of the joints microstructure, **b** microstructure in the BM, **c** MTMAZ showing elongated grains rotated compared with the BM grains, **d** boundary between MTMAZ and MSZ, **e** MSZ showing very fine DRX grains, and **f** boundary between MTMAZ and MHAZ
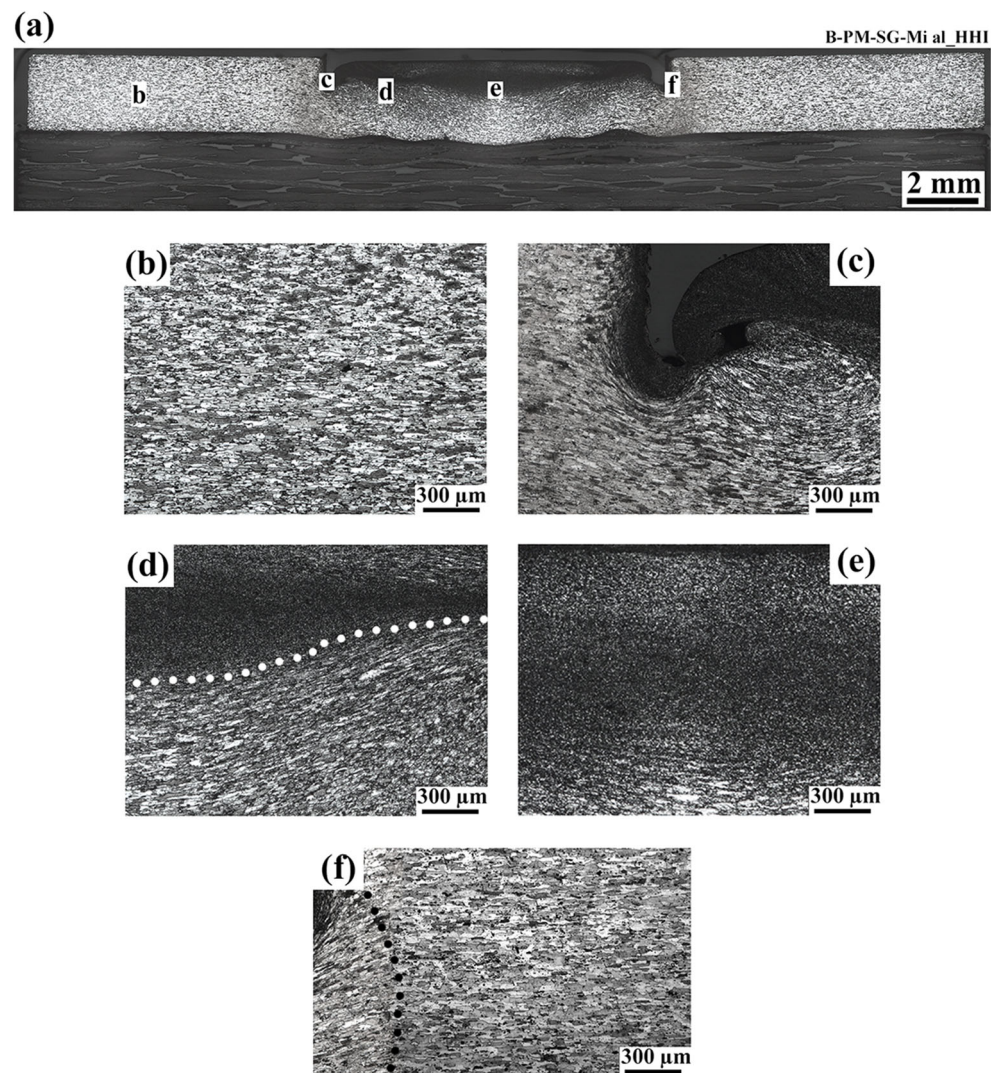
the high strain rate as a result of the tool's rotational speed as well as axial movement [25, 47, 48]. The microstructure in this zone is thus characterized by elongated grains that are rotated approximately 45° compared with unaffected grains. One can see that the grains in MTMAZ are elongated and rotated from top-left to bottom-right (Fig. 15c) compared with the AA2024 BM (Fig. 15b). The induced grain deformation in this zone may contribute to the strain hardening effect [47]. However, since the temperature and strain rate are relatively high in MTMAZ, some dynamic recovery may also occur, which reduces the strain hardening effect [49, 50]. In addition, due to the relatively high temperature achieved in this area, coarsening of the strengthening particles may also take place [51]. Therefore, the local mechanical strength of the aluminum in the MTMAZ is affected by these competing phenomena (strain hardening, dynamic recovery, and precipitation coarsening).

MSZ lies in the center of the spot that undergoes the highest strain rate as a result of the aluminum being stirred by the tool [47, 52]. The highest frictional heat generation and attained temperature is also expected in this zone [47, 52]. Dynamic recrystallization (DRX) is one the main mechanisms taking place in the MSZ in FSpW of aluminum, which leads to an equiaxed, refined grain structure [25, 47]. DRX occurs in many metallic materials above 0.6 melting point (Tm) under high stress or high deformation rates [49, 50]. High temperatures obtained during FSpJ of AA2024 / CF-PPS [22] in combination with a high strain rate due to the tool's rotational speed results in a very fine grain structure in the MSZ. Figure 15d shows the boundary between MSZ and MTMAZ, and Fig. 15e illustrates the MSZ with very fine grain structure. In addition to grain refinement, solubilization of the strengthening particles in the course of the joining cycle is expected in the MSZ as a result of the high temperature. Re-precipitation of these particles during the cooling phase is believed to increase the local strength of the MSZ [47].

MHAZ is the third zone formed during the FSpJ process between the BM and MTMAZ. In this region, the aluminum is not affected mechanically and the temperature is not as high as

Fig. 16 **a** Microstructure of an AA2024/CF-PPS joint. *Yellow dashed line* indicates the boundary between PHAZ and BM. De-consolidation defects in the composite, showing **b** voids in the consolidated molten layer and **c** fiber-matrix debonding
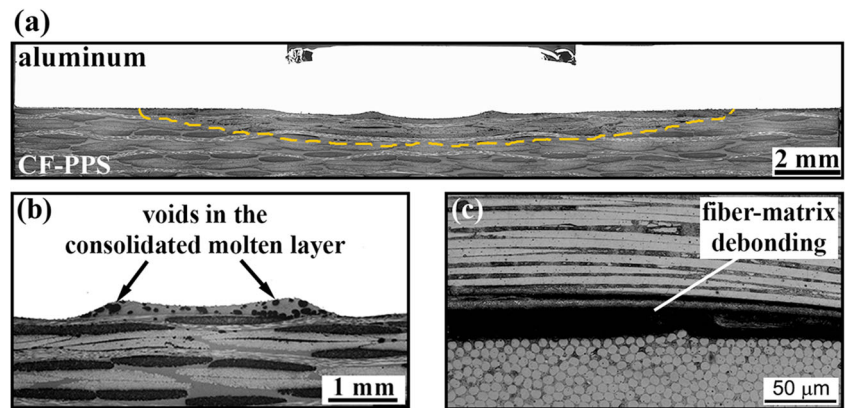
in the MSZ and MTMAZ. The moderate temperatures achieved in MHAZ may lead to the recovery phenomenon and coarsening of the strengthening particles [47]. Although such metallurgical phenomena may have occurred, no differences in grain structure could be observed between the MHAZ and BM by optical microscopy. Figure 15f illustrates the boundary between MTMAZ (left part of the figure) and MHAZ (right part of the figure).

In addition to the microstructural zones in the aluminum, a PHAZ was detected in the CF-PPS, as illustrated in Fig. 16. The yellow dashed line in the figure shows the boundary between the PHAZ and the CF-PPS base material. The conducted heat from aluminum is mainly accumulated at the interface, due to the very low thermal conductivity of PPS, which led to melting of a thin layer of PPS close to the interface. However, due to the high thermal conductivity of the carbon fibers, the heat is dissipated to some extent inside the thickness of the composite, which results in an increase in the depth of the PHAZ.

The temperature in the PHAZ was reported to be higher than the glass transition temperature (T_g) of CF-PPS (approximately 90 °C) as well as being above the T_m in the vicinity of the interface [28]. Some of the molten PPS matrix is squeezed out of the nub. In addition, the viscosity of the molten polymer is reduced, which leads to the entrapment of air pockets in the slowly flowing PPS as can be seen in Fig. 16b. As the cooling rate is very fast, these entrapped air pockets cannot escape from the PPS and remain as volumetric flaws in the joint. The main type of flaw identified in the PHAZ close to the

interface with the aluminum was reported as pores and voids [28]. The formation of voids giving rise to defects as a result of air entrapment is also detected in resistance welding [53] and laser welding [54] of thermoplastics. However, the temperature through the thickness of the composite reduces to below T_m. During the cooling phase, debonding between the PPS matrix and carbon fibers is expected (Fig. 16c) due to the large differences between the coefficients of thermal expansion of the PPS and fibers.

4.4 Local mechanical properties

Local mechanical properties in FSpJ are divided into metal properties and composite properties. Microhardness was used to evaluate the local mechanical properties of the AA2024. Nanoindentation was used to evaluate the local mechanical properties of the composite close to the interface with the aluminum.

4.4.1 AA2024-T3

Figure 17 shows microhardness map of the aluminum part. Due to microstructural symmetry around the center of the spot in FSpJ, only half of the sample was needed to generate the microhardness map. In the x-axis, 0 mm corresponds to the edge of the sample, whereas 12.5 mm is the exact center of the spot. In the y-axis, 0 mm shows the top surface of the aluminum, approaching the interface with the CF-PPS at 2 mm.

Fig. 17 Microhardness map of the AA2024 from the edge of the specimen (x = 0 mm) to the middle of the spot (x = 12.5 mm) in an AA2024/CF-PPS joint
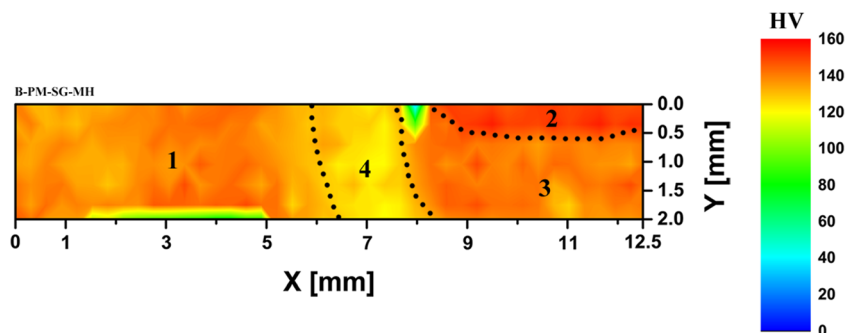
Table 2 Average and standard deviation of indentation modulus and hardness of the PPS obtained from the unloading section of the load-displacement curves

Joining condition	Modulus (GPa)	Hardness (GPa)
BM	4.7 ± 0.1	0.26 ± 0.005
Joint	5.3 ± 0.7	0.28 ± 0.03

From the microhardness map presented in Fig. 17, one observes four distinct zones, numbered in the figure. The BM (Zone 1) with an average hardness of 135 HV starts from the edge of the sample. The BM ends at a distance of approximately 6 mm from the edge of the joint. Inhomogeneous distribution of the microhardness map in this zone may be attributed to the distribution of the strengthening particles. In positions where the indenter touches or is very close to the particles, a higher value of hardness was obtained.

The MSZ (Zone 2) with higher hardness compared with the BM is obvious as the upper portion of the aluminum part inside the spot area, with an average hardness of 151 HV. The high hardness in the MSZ is related to the very fine DRX grains as well as re-precipitation of strengthening particles as explained in the previous section.

The area below the MSZ approaching the interface is a mixture of MTMAZ (Zone 3) and MHAZ with an average value of 139 HV. As explained earlier, there are three competing mechanisms taking place in the MTMAZ. From the microhardness results, it seems that strain hardening has a larger influence than dynamic recovery or precipitation coarsening, since the average hardness is higher than the BM.

Finally, the MHAZ (Zone 4) with a much lower hardness of 123 HV is visible between the BM and the beginning of the spot area. Recovery and coarsening of the strengthening particles are the primary mechanisms, leading to a reduction of hardness in the MHAZ.

It is worth mentioning that the areas in the figure with very low hardness on top of the aluminum surface and close to the interface result from indents near the embedding resin and PPS polymer, respectively.

4.4.2 CF-PPS

Nowadays, the use of nanoindentation for the mechanical evaluation of composites and nanocomposites is well established [55]. In this technique, a force-displacement curve is traditionally plotted during loading and unloading. Hardness and quasi-static elastic modulus are obtained from the unloading part of the curve, as explained by Oliver and Pharr [56]. However, measuring the hardness and stiffness by such a method is limited to the materials giving an elastic or elastic-plastic response [55, 57]. Since polymer materials possess time-dependent deformation behavior, the slope of the unloading curve usually does not represent linear elastic recovery [57] and so may not give the accurate measurements. A more advanced technique of continuous stiffness measurement (CSM) was introduced for materials with time-dependent properties [55–59]. In this technique, a sinusoidal force is superimposed on a quasi-static load during the loading segment [55, 57]. Employing the CSM technique allows dynamic evaluation of the properties as a function of the indentation depth, among other possibilities [55]. For more information on nanoindentation techniques, refer to [55–57].

The results obtained by CSM method demonstrated a slight increase in the average of both modulus and hardness of the PPS in the joint compared with the BM, as listed in Table 2 and demonstrated in Fig. 18. It was reported that the crystallinity of the joint is lower than in the BM [28] (the results are not shown in this manuscript); therefore, there must be another phenomenon responsible for the observed increase in the local mechanical properties of the PPS consolidated layer. Ovsik et al. [60] reported an increase in nanoindentation modulus and hardness of Polyamide 12 (PA12) as a result of increased cross-linking. As explained in Section 4.2 cross-linking may occur in PPS during FSpJ, which might be responsible for the higher values of modulus and hardness of the joint compared with the BM. Cross-linking increases the chain entanglement and branching points, and consequently more load is required to overcome the cross-linked structure [61]. The results of nanoindentation along with the presented results of TGA support the idea of a slight cross-linking taking place in PPS during FSpJ process. Furthermore,

Fig. 18 Comparison of the indentation **a** modulus and **b** hardness of the PPS from the BM and the joint
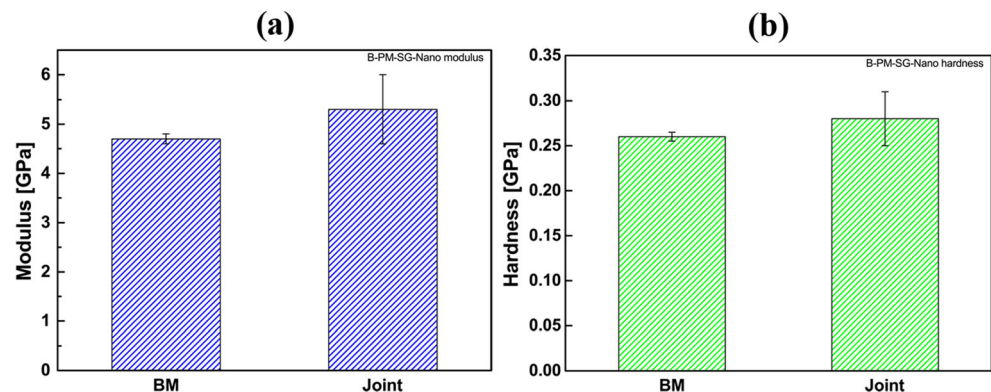
no extensive thermal degradation of the PPS is expected, because the local mechanical properties obtained from nanoindentation would otherwise be reduced compared with the BM.

4.5 Bonding mechanisms and interface analysis

"Mechanical interlocking" and "adhesion forces" are the primary bonding mechanisms in the friction spot joints. Both these bonding mechanisms can be further subdivided. Mechanical interlocking occurs on both the macro- and microlevels. Macro-mechanical interlocking is a result of polymer entrapment in the formed nub as discussed in Section 2.2. It was demonstrated that FSpJ process parameters, especially RS and PD, influence the shape and extent of the nub and therefore macro-mechanical interlocking phenomenon [22]. Micromechanical interlocking may also occur. Surface pre-treatments, particularly mechanical treatments such as sandblasting, have been used frequently to increase the surface roughness and to generate pores, crevices, and asperities. Penetration of the molten PPS into such microscale aluminum irregularities leads to the micromechanical interlocking phenomenon. Furthermore, with FSpJ, some of the fibers in the composite are entrapped by the aluminum, particularly in and around the nub region where the aluminum is plasticized and slightly deformed. Fiber entrapment is also classified under the micromechanical interlocking category.

Figure 19a, b illustrate the cross-section of a joint examined by laser scanning confocal microscopy (LSCM) showing the micromechanical interlocking phenomenon by aluminum pore and crevice filling by the molten PPS and fiber entrapment. High-magnification SEM imaging (Fig. 19c) shows that in some cases, a layer of molten PPS flows between the carbon fibers and the aluminum. Although direct contact between the aluminum and carbon fibers may improve mechanical performance of the joints by improved micromechanical interlocking, it could nonetheless prove detrimental to its corrosion behavior when exposed to a corrosive environment. Therefore, the presence of such a layer may in fact reduce the rate of corrosion.

Adhesion forces can be divided into physical and chemical bonding. Physical adsorption and bonding (as a result of weak Van der Waals forces) are believed to be present in FSpJ where the molten PPS is in intimate contact with the aluminum. In addition, strong chemical adsorption and bonding may occur between the molten polymer and the joining parts if the surface of the aluminum and/or composite is activated by suitable surface pre-treatments [21].

Various chemical and electrochemical pre-treatments were applied on the surface of AA2024-T3 to understand their influence on the interfacial bonding mechanisms and adhesion forces. Conversion coating (CC) using Alodine® 4850 was among the employed surface pre-treatments. The Alodine solution is chromium-free, contains primarily hexafluorozirconate (HFZ) [62], which produces a colorless conversion layer. Deposition of new elements on the surface of AA2024 after CC was identified by X-ray photoelectron spectroscopy (XPS) [21]. The new elements such as zirconium were able to strongly bond with the carbon from the polymer molten layer increasing the strength of the joints. To better understand the bonding mechanisms at the interface between AA2024-T3 (coated with the Alodine) and CF-PPS during the FSpJ process, the fracture surface was analyzed with XPS, and the results were recently reported in [21]. It was reported [23] before that the failure in FSp joints takes place primarily inside the PPS, and some of the PPS layer remains attached to the

Fig. 19 Cross-section of an AA2024/CF-PPS FSp joint in the PDZ examined by LSCM showing micromechanical interlocking through **a** aluminum pore/crevice filling by the molten PPS in a resin-rich area and **b** fiber entrapment (adapted from [23]). **c** High magnification SEM image showing a thin layer of the PPS between aluminum and carbon fibers
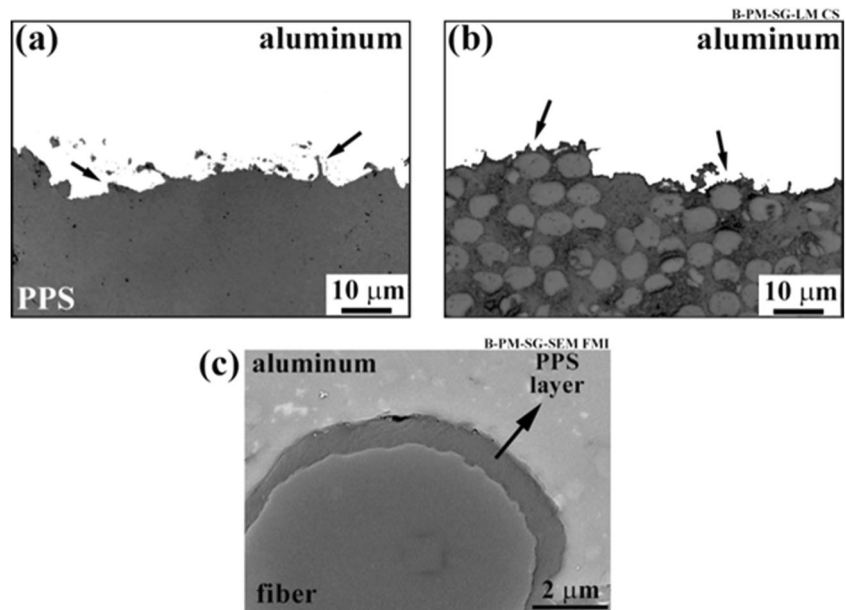
aluminum after fracture. For this reason, XPS analysis was performed on several areas of the consolidated PPS on the aluminum side of the failed specimens.

No significant differences in the resulting spectra from various areas were identified. The XPS spectra were obtained from fracture surfaces after argon etching for 1800 s to remove any possible environmental contamination (e.g., CO_2) and the majority of the adhered PPS layer to obtain information from just the interface. The obtained spectra were compared with the spectrum of the same position before argon etching. Figure 20 illustrates the high-resolution XPS spectra (C 1s and Al 2p regions) obtained for CC before and after etching for 1800 s. As can be seen from the C 1s region (Fig. 20a), a peak at approximately 284.5 eV binding energy is present both before and after etching. It has been discussed [21] that this peak is attributed to the C bonds from the PPS layer. A binding energy of 284.5 eV corresponding to the C 1s spectrum of PPS was reported to be related to carbon atoms in phenyl rings [63]. After 1800 s of argon etching, two small peaks appeared in the C 1s spectrum, one at about 282.1 eV and the other at approximately 289 eV. The first peak position is similar to the C–Zr compound reported in [64, 65].

The new peak at 289 eV is reported [21] to appear due to C-Al covalent bond formed at the interface. The C-Al bond formation may be further analyzed from the Al 2p region in Fig. 20b. Both spectra show a peak at 72.8 eV that has been reported as the peak of metallic aluminum [66, 67]. Before etching, a peak at approximately 75.8 eV can be identified, corresponding to Al–O bonds and probably from the aluminum oxide layer. Marcus et al. [68] reported the formation of an Al–O chemical bond in an aluminum-polymer system at 75.5 eV, very close to the one identified in this work. After etching, this peak became broader, which is believed to be due to the Al–C bond formation at the interface, overlapping with the existed Al–O peak. A combination of both C 1s and Al 2p spectra of the CC pre-treated specimen confirms the formation of the covalent Al–C chemical bond at the interface.

For detailed discussions on the formation of interfacial bonds and the influence of other surface pre-treatments, refer to [21, 28].

4.6 Global mechanical properties

4.6.1 Quasi-static loading

Influence of surface pre-treatment As explained before, mechanical interlocking and adhesion forces are the primary bonding mechanisms found in FSpJ. So, any alteration on the surface of the aluminum part resulted in surface topography and chemistry changes will influence the bonding mechanisms and hence the strength of the FSp joints.

The influence of various aluminum surface pre-treatments on the interfacial bonding mechanisms and mechanical performance of AA2024-T3/CF-PPS FSp joints were recently investigated [23, 28]. The surface pre-treatments varied from mechanical to chemical and electrochemical pre-treatments as well as a combination of mechanical and chemical pre-treatments. The entire aluminum surface pre-treatments increased the lap shear strength of the joints to some extent compared with the as-received (AR) condition as shown in Fig. 21.

Mechanical surface pre-treatments, such as mechanical grinding (MG) and sandblasting (SB), as well as electrochemical pre-treatments such as sulfuric acid anodizing (SAA) and phosphoric acid anodizing (PAA) increase the surface roughness of the aluminum. An increase in surface roughness is largely due to the generation of crevices, pores, and other irregularities. This leads to an improved micromechanical interlocking and therefore better shear strength of the FSp joints. As discussed in the previous section, specific surface pre-treatments such as conversion coating (CC) lead to the formation of strong chemical bonds between pre-treated aluminum and the PPS consolidated layer at the interface. Formation of such chemical bonds enhanced the adhesion forces between the joining parts, improving the shear strength of the joints. Moreover, combination of mechanical and chemical pre-treatments such as SB and CC alters both aluminum surface topography and chemistry. In such cases, both bonding mechanisms, i.e., micromechanical interlocking and adhesion forces were improved. This is in fact the reason of the better lap shear strength of the combination of surface pre-treatments compared with the individual ones, as can be seen in Fig. 21. The highest lap shear strength of approximately

Fig. 20 High-resolution XPS spectra before (*red*) and after (*black*) etching for 1800 s from **a** C 1s and **b** Al 2p regions. Reproduced with permission from [21]
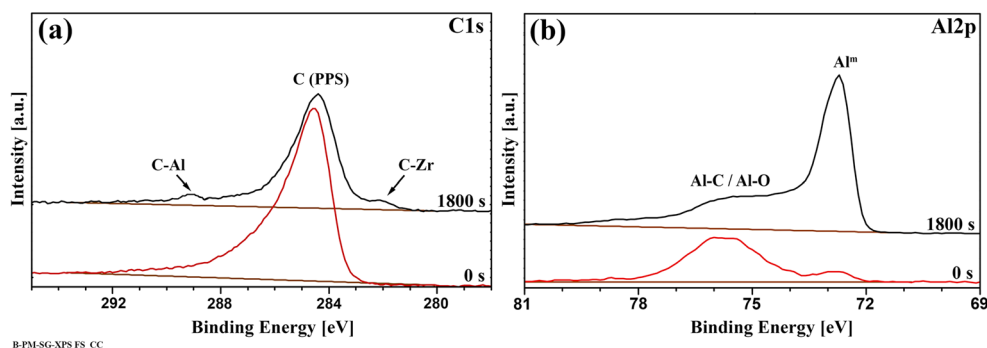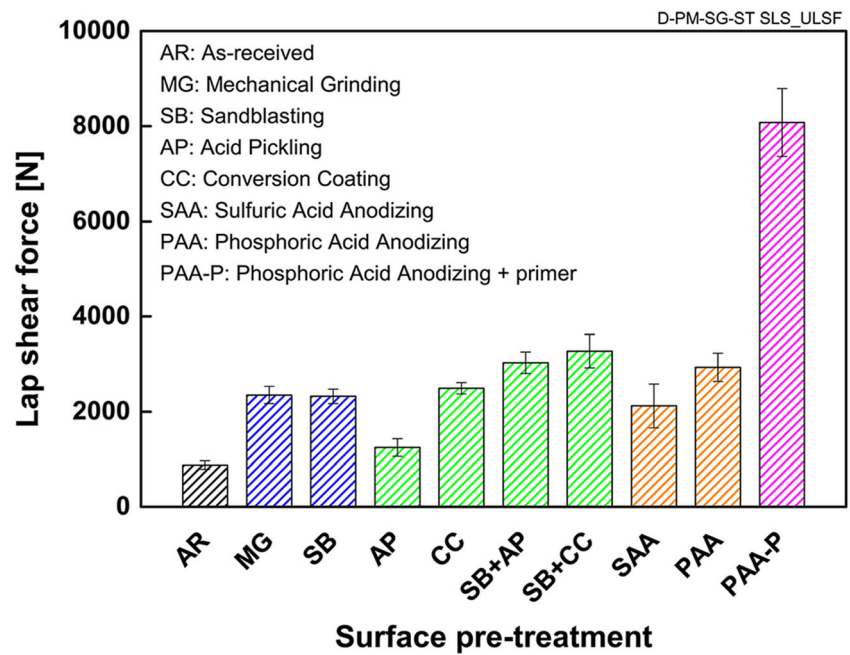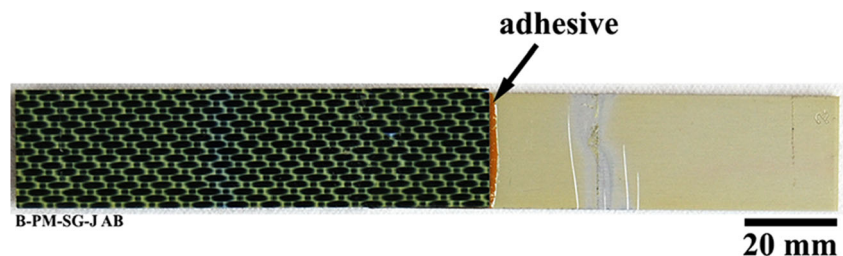
Fig. 21 Mechanical strength of single-lap shear AA2024/CF-PPS FSp joints after aluminum surface pre-treatments

8.0 ± 0.7 kN was achieved when PAA pre-treatment was followed by the application of a primer layer (PAA-P) [28]. This was explained by the fact that the primer was a carbon-based epoxy layer leading to the formation of very strong carbon-carbon primary bonds with the PPS consolidated layer during the joining cycle [28]. PAA-P pre-treatment was particularly investigated in this work because it is used commonly in the aircraft industry.

Comparison between the mechanical performance of FSp and state-of-the-art adhesively bonded joints To assess the mechanical performance of the FSp joints compared with the state-of-the-art metal-composite joining technologies, reference adhesively bonded joints were produced in accordance with the aircraft standards using the same materials used in this work. In order to provide a direct comparison, five reference single-lap shear joints with similar configuration to FSp joints (bonding area of 25 × 25 mm) were assembled using structural adhesive. Furthermore, because PAA-P is the standard surface pre-treatment in the aircraft industry, it was also selected for the reference adhesively bonded joints. However, for adhesive bonding, the composite was also pre-treated using PAA-P. This was done due to the difficulties of bonding thermoplastic composites because of their low surface tension.

It is well known that thermoplastics require physical or chemical surface modification to produce acceptable adhesively bonded joints [69]. Figure 22 shows an example of the top view of the aluminum-composite-bonded joint.

The reference-bonded joints were mechanically tested under lap shear loading similar to the FSp joints. Figure 23 shows the comparison between the lap shear strength and displacement at the peak load of FSp and reference-bonded joints. FSp joints displayed an average ultimate lap shear force (ULSF) of 8264 ± 645 N, whereas the reference-bonded joints showed an average ULSF of 5459 ± 2036 N. Moreover, the FSp joints reached an average displacement of 1.73 ± 0.13 mm, whereas the average maximum displacement reached by the reference-bonded joints was 0.92 ± 0.31 mm. Therefore, FSp joints showed an increase of 51 % in lap shear strength and 88 % in displacement compared with the state-of-the-art adhesive-bonded joints.

In addition to the better mechanical performance of FSp joints in direct comparison with adhesively bonded joints, an important characteristic of the FSpJ process is its ability to produce lighter structures, because no additional material such as adhesive is used to join the parts together. In this work, the weight reduction using FSpJ was approximately 3.4 ± 0.5 % compared with the reference adhesive bonding. The average weight of the FSp joints was 22.60 ± 0.14 g, whereas the

Fig. 22 View from above of an adhesively bonded joint between AA2024-T3 and CF-PPS pre-treated by the PAA-P procedure

Fig. 23 Comparison of the **a** lap shear strength and **b** displacement at the peak load of the FSp joints and reference-bonded joints
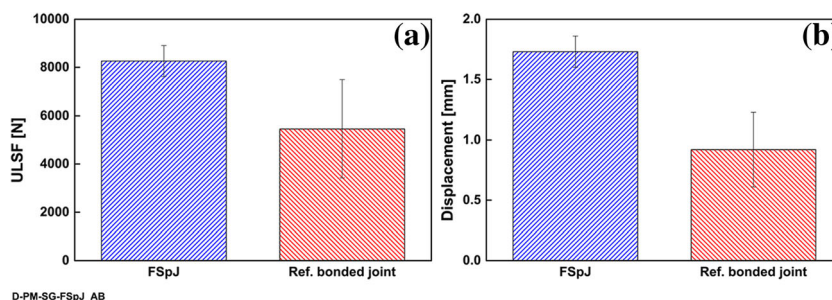
reference adhesively bonded joints weighed 23.37 ± 0.08 g. Finally, it should also be remembered that the joining time is much faster for FSpJ (4 s in this work) compared with the adhesive bonding (ranging from several minutes to several hours).

4.6.2 Dynamic loading

This section briefly describes the fatigue performance of the SLS FSp joints based on the S-N curve life analysis, under constant amplitude loading. A load ratio of $R = 0.1$ (usual in aircraft industry) and a frequency of 5 Hz was used. Four aluminum surface pre-treatments were selected to carry out the fatigue experiments; these were sandblasting (SB), sandblasting with subsequent conversion coating (SB + CC), phosphoric acid anodizing (PAA), and PAA with subsequent application of the primer (PAA-P).

The exponential model (also known as Lin-Log) was selected to compare the fatigue behavior of the pre-treated specimens. This comparison is shown in Fig. 24a. It is possible to observe that PAA-P specimens exhibited a much better fatigue performance compared with the rest of the pre-treatments. This was expected, because the quasi-static strength of the PAA-P joints was higher, as shown in Fig. 21. The other three surface pre-treatments showed a similar fatigue performance, but the SB + CC specimens performed slightly better than PAA and SB specimens. This also accords with their quasi-static strength, where SB + CC showed a higher strength than PAA and SB specimens.

One can also observe that the fatigue performance of the pre-treated specimens in the low cycle fatigue (LCF) regime (10^3 cycles) was very similar to their quasi-static strength, being much higher for the PAA-P. By contrast, in the high cycle fatigue (HCF) range (10^6 cycles) the fatigue performance of the PAA-P specimens tended to approach the other surface pre-treatments, although it remains better than the other specimens, as shown in Fig. 24a. It is known that SLS geometry has very poor resistance to shear loading due to the secondary bending effect [70, 71]. It is also reported that during fatigue testing peel stresses are generated at the edges of the joints during each cycle [70, 71]. As the applied fatigue loads were higher for the PAA-P specimens, it is believed that higher peel stresses were generated in these joints, particularly in the HCF regime. Such peel stresses reduce the fatigue performance of SLS joints. Moreover, it is well known from the principles of adhesive bonding that shear stresses are maximized (peak shear stresses) at the edges of the joint. Generally, higher applied external loads and shear modulus of the adhesive increases the peak shear stresses at the edges [72–75]. Due to the similarities between FSpJ and adhesive bonding, analogous conclusions may be drawn. Since the PAA-P specimens led to much stronger joints, compared with other surface pre-treatments, and the applied fatigue loads were also higher, it would be expected that the generated shear stresses at the edge of the joint are also higher. Increased peel stresses and peak shear stresses in the PAA-P specimens resulted in a steeper slope of the S-N curve.

The specimens that survived one million cycles of fatigue loading were subsequently tested under lap shear

Fig. 24 **a** S-N curves of the various surface pre-treatment specimens based on the exponential model and **b** quasi-static strength of the FSp joints for the surface pre-treatments after 10^6 cycles of fatigue loading compared with the respective initial quasi-static strength
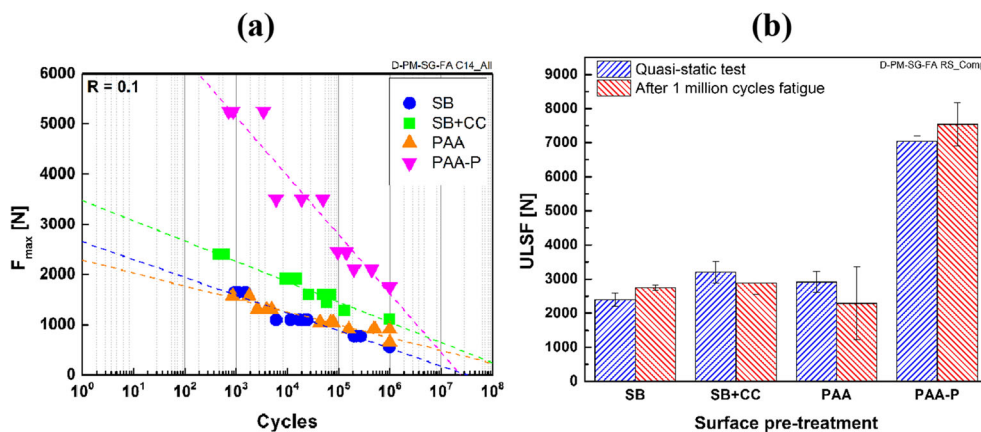
testing to obtain their residual strength. Figure 24b illustrates the comparison between initial quasi-static and residual strength of the joints after one million cycles. Surprisingly, SB and PAA-P specimens showed an average residual strength slightly higher than the initial lap shear strength by 15 and 7 %, respectively. For the SB + CC and PAA specimens, the residual strengths were lower compared with the initial strengths by 10 and 22 %, respectively. However, the standard deviation in all surface pretreatments neither the increases in strength for SB and PAA-P specimens nor the decreases for SB + CC and PAA specimens are conclusive. It is known that damage accumulation largely reduces the residual strength of composite joints [70]. So, it is believed that no damage is generated and accumulated in the FSp joints for the selected loading conditions even after one million cycles. Although it was mentioned earlier that peel stresses could be generated during the fatigue loading, which would lead to damage accumulation, it may be concluded that the induced peel stresses are negligible under these loading conditions. The fatigue shear loads were also quite low, whereby damage is not induced and accumulated. The fatigue loads under which the samples survived one million cycles correspond to 25 % of the initial lap shear strength for SB, PAA, and PAA-P specimens and 35 % for the SB + CC samples.

Figure 25 shows the SEM examination of the fracture surface of an SB specimen on the composite side after fatigue failure. Elongated PPS matrix fibrils in the warp direction along the loading direction (Fig. 25a) are an indication of ductile fracture, whereas fiber breakage and fiber-matrix debonding were the main failure micromechanisms in the weft direction (Fig. 25b). At high magnification, two types of fatigue striations could be observed; first, debonding from the fibers in the elongated PPS matrix in the weft direction (Fig. 25c), and second, in the resin-rich area between the fibers (Fig. 25d). As explained by von Bestenbostel and Friedrich [76], striations are step-like structures that can be detected using a suitable contrast origin in the SEM. Since striations are generated out of the fracture plane, a tilt angle is usually also required to identify them [76]. In the FSp joints, striations could be observed at various positions in the weft direction, but the generation of fatigue striations could not be confirmed in the warp direction.

Similar fatigue striations to those illustrated in Fig. 25c were also observed in resistance-welded thermoplastic composites [70]. The authors concluded that the striations were generated due to peel stresses perpendicular to the loading direction. The cause of this type of fatigue striation in this work appears similar, due to local out-of-plane stresses generated along the fiber-matrix interface (weft direction). It is believed that in the weft direction, the cracks propagate out-of-plane, perpendicular to the fiber-matrix interface, producing fatigue striations in the PPS. Even so, the final failure occurs due to the tearing of the PPS matrix. In the final stages, the torn matrix becomes elongated in the loading direction. The second type of striation shown in Fig. 25d is very similar to those reported in [76] in resin pockets, which are typical defects in the composites. Since there is a change in the local stiffness between the fibers and the surrounding resin, such resin pockets act as crack initiation sites during fatigue loading [76]. In FSpJ, microvoids have a similar effect to the resin pockets, acting as initiation sites for fatigue cracks. Therefore, two types of striation could be identified as micromechanisms in fatigue failure of an FSp joint.

Fig. 25 Failure micromechanisms of a high cycle fatigue SB specimen from the composite side; a warp fibers orientation, b weft fibers orientation, c fatigue striations in the PPS matrix debonding from the fibers, and d striations in the PPS matrix in a resin-rich area. Black arrows in (a) and (b) indicate the loading direction; c, d taken at a tilt angle of 45°
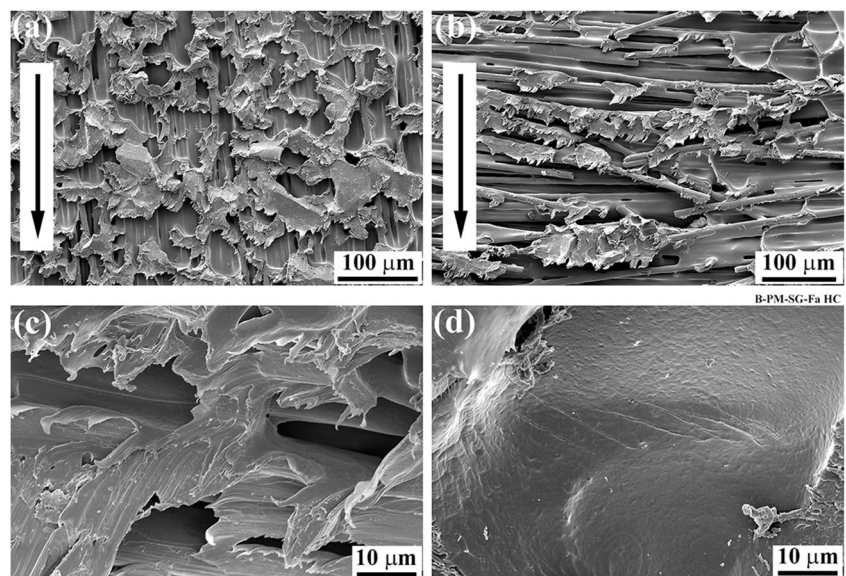
5 Conclusions

The main objective of this paper was to give a general overview on different aspects of the novel FSpJ process. The following main conclusions may be drawn from this work:

- The range of peak process temperature was far below the onset of mass loss for PPS. Extensive thermal decomposition of the composite is not expected for the optimized set of parameters. However, slight cross-linking of the PPS may occur during the process.
- Microstructure of the joint can be divided into four zones: MSZ, MTMAZ, MHAZ, and PHAZ. Similar metallurgical phenomena as FSpW of aluminum were observed in this work. In the PHAZ, defects such as pores (due to the entrapment of air in the PPS molten layer) and fiber-matrix debonding were detected.
- Local mechanical properties of the aluminum were influenced by the metallurgical changes. The hardness of the MSZ was higher than the BM, whereas MHAZ showed a lower hardness than the BM. In case of the composite, the hardness and modulus of the PPS in the joint were slightly higher than the BM. This was attributed to slight cross-linking taking place in the PPS during FSpJ.
- FSpJ showed three primary bonding mechanisms at the interface: macro-mechanical interlocking as a result of the nub formation and insertion into the composite, micromechanical interlocking due to the keying effect of the molten PPS into the pores and crevices of the aluminum as well as fiber entrapment by the deformed aluminum, and finally adhesion forces between consolidated molten PPS and aluminum.
- Certain aluminum surface pre-treatments improve the bonding mechanisms by changing aluminum surface topography and/or surface chemistry. XPS analysis showed, as an example, the formation of chemical covalent bonding between aluminum and PPS by performing conversion coating on the surface of the aluminum prior to FSpJ.
- It was shown that aluminum surface pre-treatments increasing the mechanical strength of the joints compared with the as-received condition to some extent. This was in fact due to the improvement of the bonding mechanisms. PAA-P as one of the standard surface pre-treatment in aircraft industry showed the best performance for the friction spot joints.
- Comparison between quasi-static strength of the FSp joints with the state-of-the-are adhesive bonding with identical surface pre-treatment (PAA-P) showed that FSp joints are approximately 50 % stronger. Further, FSp joints were approximately 3 % lighter than adhesively bonded joints.
- Finally, fatigue experiments showed that similar to quasi-static strength of the joints, PAA-P ensures the best fatigue performance compared with other surface pre-treatments used in this work.

Through the results obtained in this work, it is possible to propose FSpJ as an innovative and potential friction-based joining technique for lightweight structures particularly in transport industries.

Besides the raised topics in the current manuscript, other subjects such as the influence of a vast number of aluminum surface pre-treatments on the behavior of the FSp joints, the durability of the joints under harsh environmental conditions, and fatigue performance were investigated into details. Moreover, detailed investigations on the fracture micromechanisms, interfacial bonding analysis, and the mechanical performance of the joints under mode I loading were carried out. For more information, refer to [21, 24, 28].

References

1. Zhang J, Chaisombat K, He S, Wang CH (2012) Hybrid composite laminates reinforced with glass/carbon woven fabrics for lightweight load bearing structures. J Mater Des 36:75–80
2. Mallick PK (2010) Joining for lightweight vehicles. In: Mallick PK (ed) Materials, design and manufacturing for lightweight vehicles. Woodhead Publishing Ltd., Cambridge, pp. 275–308
3. Dursun T, Soutis C (2014) Recent developments in advanced aircraft aluminium alloys. J Mater Des 56:862–871
4. Li Y, Lu J (2014) Lightweight structure design for wind energy by integrating nanostructured materials. J Mater Des 57:689–696
5. Sedlacek G, Trumpf H (2007) Innovative developments for bridges using FRP composites. Woodhead Publishing Ltd., Cambridge
6. Marsh G (2014) Composites and metals—a marriage of convenience? Reinf Plast 58:38–42
7. Peters ST (1998) Handbook of composites, 2nd edn. Chapman & Hall, London
8. Airbus A350 XWB. www.a350xwb.com. Accessed 5th January 2015
9. Boeing 787 from the ground up. www.boeing.com. Accessed 5th January 2015
10. Sloan J. (2014) The making of the BMW i3. Composites World. http://www.compositesworld.com. Accessed 3rd January 2015
11. Drake N. (1998) Thermoplastics and Thermoplastic Composites in the Automotive Industry 1997–2000. Rapra Industry Analysis Report Series
12. N.N. (2014) Plastics and Polymer Composites Technology Roadmap for Automotive Markets. American Chemistry Council
13. Yancey R. (2013) Carbon fiber composites: into the automotive mainstream? High-Performance Composites, vol 21
14. Srivastava V, Srivastava R (2013) Advances in automotive polymer applications and recycling. Int J Innov Res Sci, Eng Technol 2(3): 744–746
15. Mercedes-Benz Forschungsfahrzeug F 125! www.daimler.com. Accessed 25th January 2015

16. Amancio-Filho ST, dos Santos JF (2009) Joining of polymers and polymer-metal hybrid structures: recent developments and trends. J Poly Eng Sci 49(8):1461–1476. doi:10.1002/pen.21424

17. Kinloch AJ, Kodokian GKA (1989) The adhesive bonding of thermoplastic composites. Imperial College of Science, Technology and Medicine, London

18. Amancio-Filho S.T., dos Santos, J.F. (2012) Method for joining metal and plastic workpieces. European Patent No. EP2329905B1

19. Schiling C., dos Santos, J.F. (2005) Method and device for linking at least two adjoining work pieces by friction welding. International Patent Publication WO/2001/036144

20. Amancio-Filho ST, Bueno C, dos Santos JF, Huber N, Hage E Jr (2011) On the feasibility of friction spot joining in magnesium/fiber-reinforced polymer composite hybrid structures. J Mater Sci Eng A 528:3841–3848

21. Goushegir SM, Scharnagl N, dos Santos JF, Amancio-Filho ST (2015) XPS analysis of the interface between AA2024-T3/CF-PPS friction spot joints. J Surf Interf Anal. doi:10.1002/sia.5816

22. Goushegir SM, dos Santos JF, Amancio-Filho ST (2015) Influence of process parameters on mechanical performance and bonding area of AA2024/carbon-fiber-reinforced poly(phenylene sulfide) friction spot single lap joints. J Mater Des 83:431–442

23. Goushegir SM, dos Santos JF, Amancio-Filho ST (2014) Friction spot joining of aluminum AA2024/carbon-fiber reinforced poly(phenylene sulfide) composite single lap joints: microstructure and mechanical performance. J Mater Des 54:196–206

24. Goushegir S.M., dos Santos, J.F., Amancio-Filho S.T. (2016) Failure and fracture micro-mechanisms in metal-composite single lap joints produced by welding-based joining techniques. J Comp Part A 81:121–128

25. Amancio-Filho ST, Camillo APC, Bergmann L, dos Santos JF, Kury SE, Machado NGA (2010) Preliminary investigation of the microstructure and mechanical behaviour of 2024 aluminium alloy friction spot welds. J Mater Trans 52(5):985–991

26. Suhuddin U., Campanelli L., Bissolatti M., Wang H., Verastegui R., dos Santos, J.F. A review on microstructural and mechanical properties of friction spot welds in Al-based similar and dissimilar joints. In: 1st International Joint Symposium on Joining and Welding, Osaka, Japan, 2013.

27. Esteves JV, Goushegir SM, dos Santos JF, Canto LB, Hage E Jr, Amancio-Filho ST (2014) Friction spot joining of aluminum AA6181-T4 and carbon fiber-reinforced poly(phenylene sulfide): effects of process parameters on the microstructure and mechanical strength. J Mater Des 66(Part B):437–445

28. Goushegir S.M. (2015) Friction spot joining of metal-composite hybrid structures. Dissertation, Hamburg University of Technology (TUHH), Hamburg

29. Andre, N.M., Goushegir, S.M., dos Santos, J.F., Canto, L.B., Amancio-Filho, S.T. On the microstructure and mechanical performance of friction spot joining with additional film interlayer. In: Annual Conference of the Society of Plastics Engineers, ANTEC 2014, Las Vegas (CA), 2014. pp 1811–1817

30. Huda Z, Taib NS, Zaharinie T (2009) Characterization of 2024-T3: an aerospace aluminum alloy. J Mater Chem Phys 113:515–517

31. Davis J.R. (ed) (1996) ASM International: handbook of aluminium & aluminium alloys. 3rd edn, Ohio

32. Maruszczak W. Advanced composite polymer for the automotive market; long fiber reinforced linear polyphenylene sulfide (PPS). In: SPE ACCE conference, Michigan, USA, 2007

33. N.N. (2010) Thermoplastic composites for aerospace. The IAPD magazine, vol April/May

34. Spruiell J.E., Janke C.J. (2004) A review of the measurement and development of crystallinity and its relation to properties in neat poly(phenylene sulfide) and its fiber reinforced composites. Oak Ridge National Laboratory, USA

35. ASTM E1131–08 (2008) Standard test method for compositional analysis by thermogravimetry. ASTM International

36. ASTM E384-992e1 (2005) Standard test method for microindentation hardness of material. ASTM International

37. ASTM D3163–01 (2008) Standard test method for determining strength of adhesively bonded rigid plastic lap-shear joints in shear by tension loading. ASTM International

38. Bo Y, Yanmo C, Hao Y, Bin S, Meifang Z (2009) Kinetics of the thermal degradation of Hyperbranched poly(phenylene sulfide). J Appl Polym Sci 111:1900–1904

39. Li XG, Huang MR, Bai H, Yang YL (2002) High-resolution thermogravimetry of polyphenylene sulfide film under four atmospheres. J Appl Polym Sci 83:2053–2059

40. Lopez LC, Wilkes GL (1989) Poly(p-phenylene sulfide)—an overview of an Impotrant engineering thermoplastic. J Macromolecular Sci, Part C: Polymer Reviews 29(1):83–151

41. Ma CCM, Hsia HC, Liu WL, Hu JT (1987) Thermal and rheological properties of poly(phenylene sulfide) and poly(ether Etherketone) resins and composites. J Poly Comp 8(4):256–264

42. Port A.B., Still R.H. (1980) Synthesis and characterization of poly(Arylene Sulphides)—part 4. Curing and degradation studies. J Poly Degradation Stability 2:1–22

43. Bauernhuber A, Markovits T (2014) Investigating thermal interactions in the case of laser assisted joining of PMMA plastic and steel. Phys Procedia 56:811–817

44. Velthuis R. (2007) Induction welding of fiber reinforced thermoplastic polymer composites to metal. Dissertation, vol. 75, IVW, Kaiserslautern

45. Day M, Budgell DR (1992) Kinetics of the thermal degradation of poly(phenylene sulfide). J Thermochimica Acta 203:465–474

46. Gros C, Tarrieu J, Nassiet V, Dutarde E (2010) A study of mechanisms of poly (phenylenesulfide) thermal degradation in air. J Adv Mater Res 112:9–17

47. Rosendo T, Parra B, Tier MAD, da Silva AAM, dos Santos JF, Strohaecker TR, Alcântara NG (2011) Mechanical and microstructural investigation of friction spot welded AA6181-T4 aluminium alloy. J Mater Des 32:1094–1100

48. Hancock R (2004) Friction welding of aluminum cuts energy costs by 99 %. Weld J 83(2):40

49. Laughlin DE, Hono K (eds) (2014) Physical metallurgy, vol 3, Fifth edn. Elsevier, Oxford

50. Cahn RW, Haasen P (eds) (1996) Physical metallurgy, Fourth edn. Elsevier, Amsterdam

51. Olea C.A.W. (2008) Influence of energy input in friction stir welding on structure evolution and mechanical behaviour of precipitation–hardening in aluminium alloys (AA2024-T351, AA6013-T6 and Al–Mg–Sc). Dissertation, University of Bochum, Bochum

52. Gerlich A, Avramovic-Cingara G, North TH (2006) Stir zone microstructure and strain rate during Al 7075-T6 friction stir spot welding. J Metal Mater Trans A 37:2773–2786

53. Ageorges C, Ye L, Hou M (2000) Experimental investigation of the resistance welding of thermoplastic-matrix composites. Part II: optimum processing window and mechanical performance. J Compos Sci Tech 60:1191–1202

54. Amanat N, Chaminade C, Grace J, McKenzie DR, James NL (2010) Transmission laser welding of amorphous and semi-crystalline poly-ether–ether–ketone for applications in the medical device industry. J Mater Des 31:4823–4830

55. Díez-Pascual AM, Gómez-Fatou MA, Ania F, Flores A (2015) Nanoindentation in polymer nanocomposites. J Prog Mater Sci 67:1–94

56. Oliver WC, Pharr GM (1992) An improved technique for determining hardness and elastic modulus using load and displacement sensing indentation experiments. J Mater Res 7(6):1564–1585

57. Gibson RF (2014) A review of recent research on nanoindentation of polymer composites and their constituents. J Compos Sci Tech 105:51–65

58. Oliver W.C., Pethica J.B. (1989) Method for continuous determination of the elastic stiffness of contact between two bodies. U.S. Patent No. 4, 848, 141

59. Pethica J.B., Oliver W.C. (1989) Mechanical properties of nanometer volumes of material: use of the elastic response of small area indentations. In: Bravman J.C., Nix W.D., Barnett D.M., Smith D.A. (eds) Thin films: stresses and mechanical properties, vol 130. Mater Res Soc, Pittsburgh, pp 13–23

60. Ovsik M, Manas D, Manas M, Stanek M, Bednarik M, Kratky P, Mizera A (2013) Nano-indentation hardness of PA12 after cross-linking due to Beta radiation. In: Zak A, Slaby A (eds) Recent advances in automatic control. Information and Communications, Valencia, Spain, pp. 145–149

61. Amancio Filho S.T. (2007) Friction riveting: development and analysis of a new joining technique for polymer-metal multi-materials structures. Dissertation, Hamburg University of Technology, Hamburg

62. N.N. (2014) Alodine 4850 Sicherheitsdatenblatt gemäß Verordnung (EG) Nr. 1907/2006. Henkel Co (in German)

63. Shimizu H, Tanabe Z, Kanetsuna H (1986) X-ray photoelectron spectroscopy of electron acceptor doped poly(p-phenylene sulfide). Polym J 18(4):367–370

64. Kaufmann R, Klewe-Nebenius H, Moers H, Pfennig G, Jenett H, Ache HJ (1988) XPS studies of the thermal behaviour of passivated Zircaloy-4 surfaces. J Surf Interf Anal 11(10):502–509

65. NIST X-ray Photoelectron Spectroscopy Database, Version 4.1 (2012) National Institute of Standards and Technology, Gaithersburg. Accessed 19.12.2014

66. So KP, Biswas C, Lim SC, An KH, Lee YH (2011) Electroplating formation of Al–C covalent bonds on multiwalled carbon nanotubes. J Synthetic Metals 161:208–212

67. So KP, Lee IH, Duong DL, Kim TH, Lim SC, An KH, Lee YH (2011) Improving the wettability of aluminum on carbon nanotubes. J Acta Materialia 59:3313–3320

68. Marcus P, Hinnen C, Imbert D, Siffre JM (1992) An in situ XPS study of the formation of aluminium-polymer interfaces. J Surf Interf Anal 19:127–132

69. Messler RW Jr (2004) Joining of materials and structures: from pragmatic process to enabling technology. Elsevier, Burlington

70. Dube M, Hubert P, Gallet JNAH, Stavrov D, Bersee HEN, Yousefpour A (2008) Fatigue performance characterisation of resistance-welded thermoplastic composites. J Comp Sci Technol 68:1759–1765

71. Quaresimin M, Ricotta M (2006) Fatigue behaviour and damage evolution of single lap bonded joints in composite material. J Comp Sci Technol 66:176–187

72. da Silva LFM, das Neves PJC, Adams RD, Spelt JK (2009) Analytical models of adhesively bonded joints—part I: literature survey. Int J Adhes Adhes 29:319–330

73. da Silva LFM, das Neves PJC, Adams RD, Wang A, Spelt JK (2009) Analytical models of adhesively bonded joints—part II: comparative study. Int J Adhes Adhes 29:331–341

74. Goland M, Reissner E (1944) The stresses in cemented joints. J Appl Mech 11:A17–A27

75. Volkersen O (1938) (in German)) die Nietkraftverteilung in zugbeanspruchten Nietverbindungen mit konstanten Laschenquerschnitten. Luftfahrtforschung 15:41–47

76. von Bestenbostel W., Friedrich K. (2009) The appearance of fatigue striations in the SEM. Paper presented at the 17th International Conference on Composite Materials, ICCM-17, Edinburgh, UK